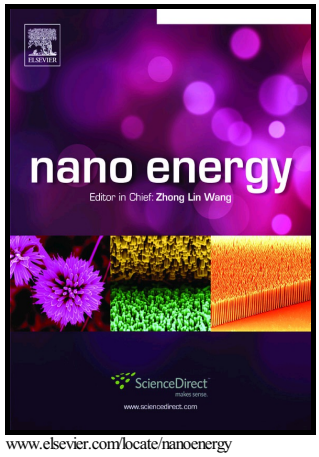

www.elsevier.com/locate/nanoenergy

A Quaternary Sodium Superionic Conductor - $Na_{10.8}Sn_{1.9}PS_{11.8}$

Zhaoxin Yu, Shun-Li Shang, Yue Gao, Daiwei Wang, Xiaolin Li, Zi-Kui Liu, Donghai Wang

PII: S2211-2855(18)30055-7
DOI: https://doi.org/10.1016/j.nanoen.2018.01.046
Reference: NANOEN2482

To appear in: *Nano Energy*

Received date: 14 December 2017
Revised date: 26 January 2018
Accepted date: 27 January 2018

Cite this article as: Zhaoxin Yu, Shun-Li Shang, Yue Gao, Daiwei Wang, Xiaolin Li, Zi-Kui Liu and Donghai Wang, A Quaternary Sodium Superionic Conductor - $Na_{10.8}Sn_{1.9}PS_{11.8}$, *Nano Energy*, https://doi.org/10.1016/j.nanoen.2018.01.046

A Quaternary Sodium Superionic Conductor - $Na_{10.8}Sn_{1.9}PS_{11.8}$

Zhaoxin Yu[a], Shun-Li Shang[b], Yue Gao[c], Daiwei Wang[a], Xiaolin Li[d], Zi-Kui Liu[b,] *, and Donghai Wang[a,] *

[a]Department of Mechanical and Nuclear Engineering, The Pennsylvania State University, University Park, Pennsylvania 16802, United States

[b]Department of Materials Science and Engineering, The Pennsylvania State University, University Park, Pennsylvania 16802, United States

[c]Department of Chemistry, The Pennsylvania State University, University Park, Pennsylvania 16802, United States

[d]Energy & Environment Directorate, Pacific Northwest National Laboratory, Richland 99352, United States

Corresponding Author

*E-mail: dwang@psu.edu

*E-mail: dr.liu@psu.edu

ABSTRACT:

Sulfide-based Na-ion conductors are promising candidates as solid-state electrolytes (SSEs) for fabrication of solid-state Na-ion batteries (NIBs) because of their high ionic conductivities and low grain boundary resistance. Currently, most of the sulfide-based Na-ion conductors with high conductivities are focused on Na_3PS_4 phases and its derivatives. It is desirable to develop Na-ion conductors with new composition and crystal structure to achieve superior ionic conductivities. Here we report a new quaternary Na-ion conductor, $Na_{10.8}Sn_{1.9}PS_{11.8}$, exhibiting a high ionic conductivity of 0.67 mS cm^{-1} at 25 °C. This high ionic conductivity originates from the presence of a large number of intrinsic Na-vacancies and three-dimensional Na-ion conduction pathways, which has been confirmed by single-crystal X-ray diffraction and first-principles calculations. The $Na_{10.8}Sn_{1.9}PS_{11.8}$ phase is further evaluated as an electrolyte in a Na-Sn alloy/TiS_2 battery, demonstrating its potential application in all-solid-state NIBs.

Key words: solid-state electrolyte, sodium-ion conductor, sodium-ion battery, single crystal X-ray

1. INTRODUCTION

Na-ion batteries (NIBs) are considered as alternatives for Li-ion batteries because of the similar electrochemistry, great abundance and wide distribution of Na resource, and huge cost advantage [1-9]. Conventional organic liquid electrolytes for NIBs can raise severe safety concerns due to their volatile and flammable nature and the high reactivity of Na metal or Na anode at low potentials [10-14]. Replacing organic liquid electrolytes with solid-state electrolytes (SSEs) is believed to address these severe safety issues of NIBs [15-21]: however, the challenges in developing Na-ion SSEs are significant.

Ceramic oxide and glass-ceramic sulfide Na-ion conductors have been explored as potential candidates for SSEs. Among the ceramic oxides, NASCON-type SSE ($Na_{1+x}Zr_2Si_xP_{3-x}O_{12}$ with $0 \leqslant x \leqslant 3$) and β”-alumina possess high room-temperature ionic conductivities over 1 mS cm^{-1} [22-26]. However, the difficulties to process ceramic oxides into electrode structures due to the harsh synthesis conditions (e.g., high synthesis/annealing temperature of over 1000 ºC) and poor electrode material-electrolyte interfacial contacts continue to make their application in batteries challenging [27-29]. Compared to ceramic oxides, sulfides SSEs are soft in nature and have low grain boundary resistance, which can facilitate the integration with electrode materials into batteries by simple cold/hot pressing [30, 31]. A glass-ceramic sulfide with cubic Na_3PS_4 crystals has been reported for use in solid-state NIBs with a high room-temperature ionic conductivity of 0.2~0.4 mS cm^{-1} [24, 32]. Based on the same crystal structure as Na_3PS_4, cation or anion substitution/doping has been adopted to further boost the room-temperature ionic conductivities [33-39]. Departing from the crystal structure of Na_3PS_4, a new family Na-ion conductor of $Na_{10}MP_2S_{12}$ (M=Si, Ge, and Sn), following the similar composition of Li quaternary superionic conductor $Li_{10}MP_2S_{12}$ (M=Si, Ge, and Sn) [15, 18, 40], was theoretically predicted with high ionic conductivities (e.g., 0.94 mS cm^{-1} for $Na_{10}SnP_2S_{12}$) at room temperature although the pure phase has not been experimentally reported. [23, 41].

Here we report a new quaternary Na superionic conductor, $Na_{10.8}Sn_{1.9}PS_{11.8}$, with a crystal structure in space group $I4_1/acd$. This new phase has a large number of intrinsic Na-vacancies and multiple Na-ion conduction pathways, thus exhibiting a high ionic conductivity of 0.67 mS cm^{-1} at 25 °C. The $Na_{10.8}Sn_{1.9}PS_{11.8}$ phase is both thermodynamically and dynamically stable according to first-principles and phonon calculations. It was also evaluated in terms of

electrochemical stability and used as an electrolyte in a solid-state Na-Sn alloy/TiS_2 battery. The promising electrochemical performance in the solid-state NIB demonstrates potential applications of this new Na-ion conductor.

2. Material and methods

Synthesis. Na_3PS_4, $Na_{10}SnP_2S_{12}$, $Na_{10.5}Sn_{1.5}P_{1.5}S_{12}$, and $Na_{10.8}Sn_{1.9}PS_{11.8}$ were prepared by heating the stoichiometric amounts of Na_2S (anhydrous, Alfa Aesar), phosphorus lump (Alfa Aesar, 99.999%), Sn (Alfa Aesar, 99.995%) and S (Sigma Aldrich, 99.998%) in an evacuated quartz tube to 700 °C (0.5 °C/min). It was kept at 700 °C for 48 hours before cooling down to room temperature at the rate of 0.1 °C/min. Brown-colored single crystal of $Na_{10.8}Sn_{1.9}PS_{11.8}$ was picked out for crystal structure analysis.

Single crystal X-ray measurement. The X-ray data-sets were collected on a Bruker SMART APEX diffractometer equipped with fine focus Molybdenum X-ray tube (1600 kW, detector at 5.8 cm, φ and ω scan) at room temperature. Software programs that were used for data collection: SMART (Bruker, 2001); cell refinement: SAINT (Bruker, 2001); data reduction: SAINT and SADABS; solve and refine the structure: OLEX2. Further details of the crystal structure could be obtained from FIZ Karlsruhe with deposition number CSD-433839.

Characterization of solid electrolytes. Powder X-ray diffraction measurements were performed on a Rigaku Miniflex II spectrometer with Cu K_α radiation. An XRD holder with Beryllium window (Rigaku Corp.) was used for protecting air-sensitive materials. The Rietveld refinement was performed using the JADE 2010 software (Materials Data Corp., California) with polynomial background fitting model at the order of 5. The cross-section morphology of the SSE pellet was investigated using scanning electron microscope (Nano630 FE-SEM). The elemental ratio was determined by inductively coupled plasma emission spectrometry (ICP-AES, Perkin-Elmer Optima 5300). For measurement of ionic conductivities, the carbon-coated aluminum foil, served as blocking electrodes, was pressed onto both faces of the cold-pressed $Na_{10.8}Sn_{1.9}PS_{11.8}$ pellet under a pressure 400 MPa. The thickness of pellet was 0.7~1.0 mm, measured by stainless steel digital caliper. The 2016-type coin cell was assembled in the glovebox by sandwiching the

pellet between two stainless-steel discs as current collectors. The a.c. impedance was measured between -60 to 80 °C in the frequency range of 1 MHz to 1 Hz with an amplitude of 5 mV using Solartron 1260. Electronic conductivity was investigated by the Hebb-Wagner polarization method. Cyclic voltammetry of Na/$Na_{10.8}Sn_{1.9}PS_{11.8}$/Sn was measured with the Na metal as counter/reference electrode and Sn as working electrode with a scan rate of 0.1 mV s^{-1} from -0.5 V to 5 V (vs. Na^+/Na) at 80 °C. For XPS depth profiling, a 20 eV Ar^+ beam with a scan area of 20*20 um^2 was used. The pristine sample and the sample after CV scan were loaded in a glovebox filled with Ar gas and transferred into the instrument (*Physical Electronics VersaProbe II*) through a vacuum transfer vessel.

Battery performance Characterization. All-solid-state Na-ion battery was fabricated by pressing Na-Sn alloy foil and TiS_2 power (Sigma-Aldrich, 99.9%) onto two faces of the pressed Na_3PS_4-$Na_{10.8}Sn_{1.9}PS_{11.8}$ bilayer pellet. The obtained pellet was assembled into a 2032-type coin cell with stainless-steel discs as current collectors. All the processes were under an Ar atmosphere. The cell was cycled galvanostatically at a current density of 4.8 mA g^{-1} (0.02 C, based on the theoretical capacity of TiS_2), within the voltage range from 1.17 to 2.4 V using a BTS-5V1mA Neware battery test system. The mass loading of TiS_2 in the full cell is 0.8 mg cm^{-2}.

First-principles, phonon and AIMD calculations. The structure of $Na_{10.8}Sn_{1.9}PS_{11.8}$ for density functional theory (DFT) based first-principles calculations were simplified by $Na_{11}Sn_2PS_{12}$, where the positions of Na-vacancies were determined by examining all possible configurations and further refined by the USPEX code [42], see Supplementary Tables S3 and S4. All DFT-based first-principles, phonon, and AIMD calculations were performed by the Vienna *Ab initio* Simulation Package (VASP) [43] in terms of various exchange-correlation functionals. Phonon calculations were performed by a parameter-free mixed-space approach as implemented in our YPHON code [44]. AIMD simulations were performed for $Na_{11}Sn_2PS_{12}$ using the VASP code in terms of a canonical ensemble at several temperatures. Thermodynamic properties of Na_3PS_4, Na_4SnS_4, $Na_{11}Sn_2PS_{12}$, (and $Na_{10}SnP_2S_{12}$) were determined by the quasi-harmonic approach by first-principles and phonon calculations [45]. More details together with first-principles, phonon, and AIMD results are shown in Supplementary Materials including the employed $Na_{11}Sn_2PS_{12}$ structures (for VASP calculations), structural properties, phase stability of $Na_{11}Sn_2PS_{12}$ via

phonon density of states and thermodynamic properties at finite temperatures, and diffusion coefficients as well as activation energies of Na-ion in $Na_{11}Sn_2PS_{12}$ via AIMD simulations.

3. Results

Crystal structure of $Na_{10.8}Sn_{1.9}PS_{11.8}$ electrolytes. $Na_{10.8}Sn_{1.9}PS_{11.8}$ was synthesized by heating stoichiometric quantities of Na_2S, Sn, P and S at 700 °C in an evacuated quartz tube (see details in *Experimental* section). **Figure 1**a shows an X-ray diffraction (XRD) pattern of as-synthesized powder product of the $Na_{10.8}Sn_{1.9}PS_{11.8}$. The Rietveld refinement was conducted with respect to a new crystal structure obtained from single crystal X-ray diffraction (see below). The calculated R-Bragg factor as low as 5.07% indicates that the phase-pure $Na_{10.8}Sn_{1.9}PS_{11.8}$ powder was successfully synthesized.

The composition and crystal structure of $Na_{10.8}Sn_{1.9}PS_{11.8}$ were determined by single-crystal X-ray diffraction at 298 K with data collection and refinement details summarized in Supplementary Table S1. The chemical formula from single-crystal X-ray diffraction is assigned to be $Na_{10.8}Sn_{1.9}PS_{11.8}$. The ratio among four elements in the obtained $Na_{10.8}Sn_{1.9}PS_{11.8}$ powder was found to be Na:Sn:P:S = 10.13:1.91:0.96:11.8 by the inductively coupled plasma (ICP) spectroscopy, in good agreement with the results from single crystal X-ray diffraction. This new phase has a tetragonal structure with space group $I4_1/acd$ (no. 142) with the measured lattice parameters a = 13.5876(12) Å and c = 27.155(5) Å. Atom Sn occupies Wyckoff position 16e with site occupancy factor (sof) of 0.95; P in Wyckoff position 8a with sof = 1; S in three kinds of Wyckoff positions 32g with sof ~ 1. The distributions of Na atoms are more complicated over six Wyckoff positions, i.e., 32g (Na1 with sof ~ 0.83), 16f (Na2 with sof ~ 0.98), 16c (Na3 with sof ~ 0.93), 16d (Na4 with sof ~ 0.82), 16e (Na5 with sof ~ 0.95), and 8b (Na6 with sof ~ 0.12). Details of atomic occupancy are summarized in Supplementary Table S2.

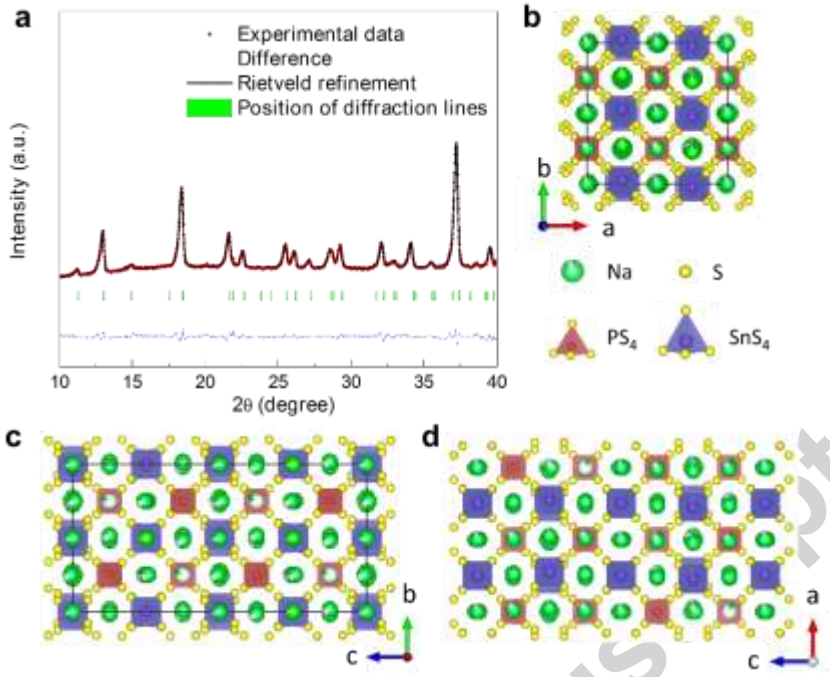

Figure 1. Crystal Structure of $Na_{10.8}Sn_{1.9}PS_{11.8}$. a) Powder X-ray diffraction pattern of the as prepared $Na_{10.8}Sn_{1.9}PS_{11.8}$ and the Rietveld refinement with respect to the single-crystal X-ray structure data. The red dot and black solid line represent the experimental data and refined pattern, respectively. The vertical green bars correspond to the expected positions of Bragg reflections of tetragonal $Na_{10.8}Sn_{1.9}PS_{11.8}$ according to the single-crystal X-ray structure data. The blue line at the bottom is the difference between experimental and refined patterns. The refined fact R-Bragg = 5.07%. b-d) Crystal Structure of $Na_{10.8}Sn_{1.9}PS_{11.8}$. Different views of the single-crystal X-ray structure of $Na_{10.8}Sn_{1.9}PS_{11.8}$. The white color in Na sphere indicates the ratio of vacancies. The schematic illustration was drawn using the program VESTA [46].

Figure 1b-d shows that the $Na_{10.8}Sn_{1.9}PS_{11.8}$ phase possesses considerable Na-ion conduction channels along such as the *a*-, *b*-, and *c*-axis directions formed by the PS_4 and SnS_4 tetrahedrons, revealed also by the AIMD simulations as shown in Supplementary Figure S1b. The partial occupancy at Na positions, such as Na1, Na4, and Na6, provides a large number of vacancies (16.9 % Na-vacancies; see Table S2). In addition, it is found that the Na positions with smaller sof (e.g., Na1, Na4 and Na6) are the neighbors of the ones with larger sof (e.g., Na2, Na3, and Na5). Both of the two phenomena are believed to promote a vacancy driven Na-ion migration [47, 48].

Ionic and electronic conductivity of $Na_{10.8}Sn_{1.9}PS_{11.8}$ electrolyte. To measure ionic conductivities of the $Na_{10.8}Sn_{1.9}PS_{11.8}$, 2016-type coin cell was assembled by sandwiching

$Na_{10.8}Sn_{1.9}PS_{11.8}$ between two stainless steel discs (as current collectors). A high pellet density indicates good and intimate contact between particles, which is the key to achieve a high ionic conductivity by minimizing the grain boundary and contact resistance. It is well known that pellet density will increase with raising pelletizing pressure [49]. In our case, a high pressure of 400 MPa has been applied to make the $Na_{10.8}Sn_{1.9}PS_{11.8}$ pellet and achieve a high density of 1.87 g cm^{-3}, as high as 80% with respect to its theoretical density obtained from single crystal X-ray diffraction. Cross-section scanning electron microscopy (SEM) image of the obtained $Na_{10.8}Sn_{1.9}PS_{11.8}$ pellet (Supplementary Figure S5) shows intimate contact between the compact particles, reflecting its high density. **Figure 2** shows impedance spectra of the $Na_{10.8}Sn_{1.9}PS_{11.8}$ within a temperature range between -60 to 80 °C and a corresponding Arrhenius plot. The impedance plots consist of a semicircle at the high-frequency region and a spike at the low-frequency region, corresponding to the contributions from total resistance (bulk/grain and grain boundary resistance) and the Al electrode, respectively. The total resistance R (bulk/grain and grain boundary resistance) was obtained from an intercept crossed between the semicircle and the spike at the x-axis in impedance plots. The ionic conductivity was calculated according to the equation $\sigma=C/R$, where $C=d/A$ is the ratio of the pellet thickness d to the area A. As-prepared $Na_{10.8}Sn_{1.9}PS_{11.8}$ sample possesses an ionic conductivity of 0.67 mS cm^{-1} at 25 °C with an activation energy (Q^{Expt}) of 0.307 eV, agreeing well with the present AIMD results with Q^{AIMD} = 0.272 ~ 0.333 eV (Supplementary Figure S4). The electronic conductivity of $Na_{10.8}Sn_{1.9}PS_{11.8}$ was evaluated by the Hebb-Wagner method using asymmetric cell (-) $Na/Na_{10.8}Sn_{1.9}PS_{11.8}/Al$ (+) at 25 °C, where carbon-coated aluminum (Al) foil served as ionic blocking electrode [50]. The total electronic conductivity (electron + hole) was calculated to be 7.17×10^{-9} S cm^{-1} at the irreversible interface $Na_{10.8}Sn_{1.9}PS_{11.8}/Al$ by linear fitting between 2 V to 4 V (Supplementary Figure S6).

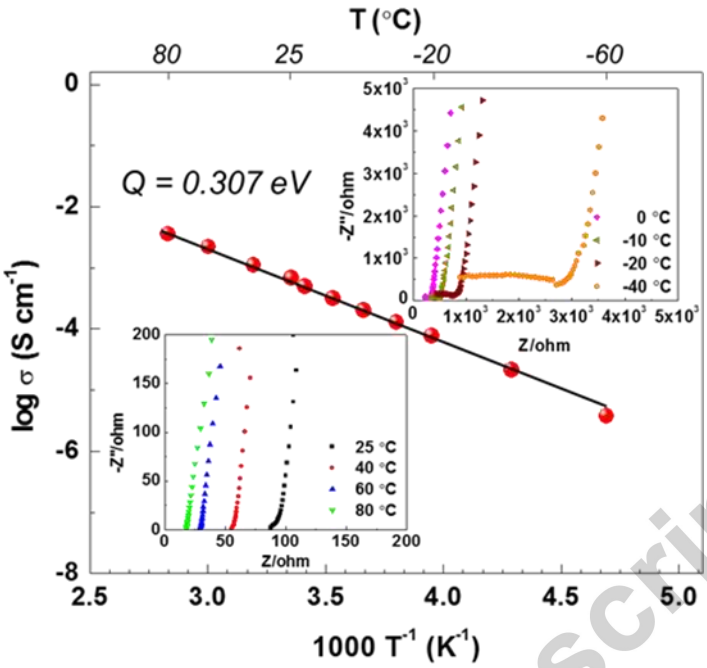

Figure 2. Ionic conductivity of $Na_{10.8}Sn_{1.9}PS_{11.8}$. Nyquist plots of the impedance and Arrhenius conductivity plot for $Na_{10.8}Sn_{1.9}PS_{11.8}$ from -60 to 80 ºC.

Electrochemical properties of $Na_{10.8}Sn_{1.9}PS_{11.8}$ SSE. Electrochemical stability of $Na_{10.8}Sn_{1.9}PS_{11.8}$ was examined from cyclic voltammetry (CV) of Na/$Na_{10.8}Sn_{1.9}PS_{11.8}$/Sn cell, with Na as the counter/reference electrode and Sn as the working electrode at 80°C. As shown in **Figure 3**a, both cathodic and anodic currents are observed near 0 V vs. Na^+/Na, corresponding to sodiation with and desodiation from Sn, respectively. No obvious oxidation current has been detected up to 5 V. However, an obvious cathodic current centered at ~ 0.32 V is detected in the CV curve, which suggests poor reduction stability of $Na_{10.8}Sn_{1.9}PS_{11.8}$ against Na metal. The stability can be improved by surface modification and the work is undergoing.

The surface of $Na_{10.8}Sn_{1.9}PS_{11.8}$ pellet contacting with Na metal after the CV scan was investigated by X-ray photoelectron spectroscopy (XPS). The XPS depth profiling (Figure 3b-d) was conducted to show surface composition changes upon the CV scan of $Na_{10.8}Sn_{1.9}PS_{11.8}$. The Na 1s signal does not show any significant changes after the CV scan. By contrast, a new peak is observed in the S 2p spectra indicating the formation of new species. Figure 3e further compares S 2p XPS spectra of $Na_{10.8}Sn_{1.9}PS_{11.8}$ before and after the CV scan. A new peak located at ~159

eV shows up after CV scan, which could be assigned to S species in Na_2S, the decomposition product after $Na_{10.8}Sn_{1.9}PS_{11.8}$ reacting with Na metal. A similar reaction is also observed for Na_3PS_4 in contact with deposited Na metal [51]. In addition, the peak associated with reduced Sn species is detected at lower binding energy in the Sn 3d spectra (Figure 3f), which is similar to the reaction for $Li_{10}GeP_2S_{12}$ in contact with Li metal, where reduced Ge species formed [52]. The XPS depth profiles of the pristine sample, as seen in Figure S7, show that the Na 1s, S 2s, and Sn 3d signals remain the same upon Ar ion sputtering, eliminating the possibility that Ar ion sputtering causes the XPS spectra change of S and Sn.

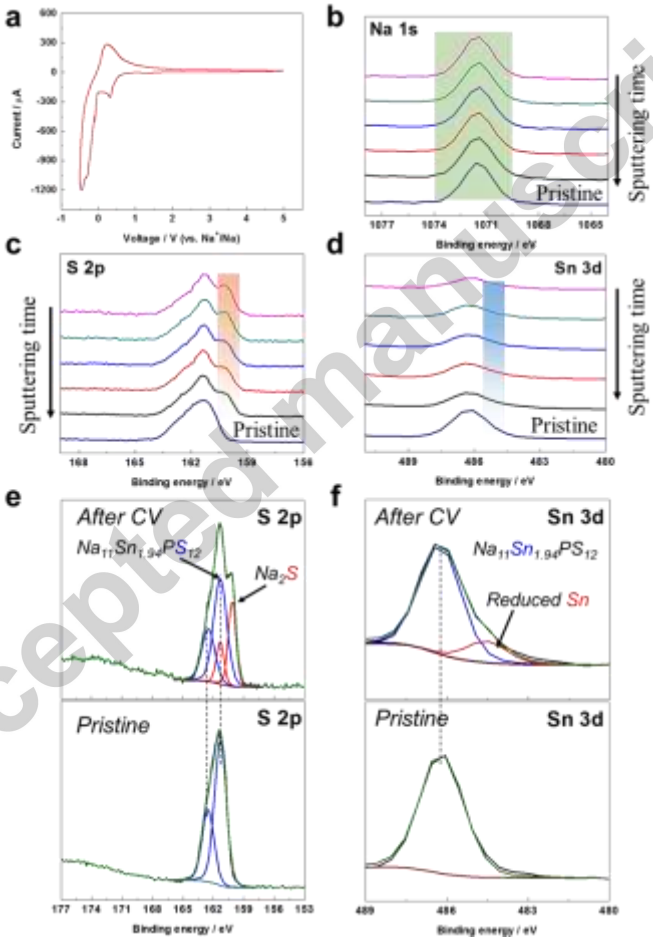

Figure 3. Electrochemical stability of $Na_{10.8}Sn_{1.9}PS_{11.8}$. a) Cyclic voltammetry of $Na/Na_{10.8}Sn_{1.9}PS_{11.8}/Sn$. The cell was characterized at 80 °C under the rate of 0.1 mV s^{-1} between -0.5 and 5 V. XPS depth profile of surface of $Na_{10.8}Sn_{1.9}PS_{11.8}$ pellet after the CV scan. b) Na 1s, c) S 2p, and d) Sn 3d signals are displayed for different sputtering time (top curve (before sputtering), in steps of 30 sec). The spectra of pristine sample before the CV scan are attached at the bottom for comparison. XPS detail spectra of e) S 2p and f) Sn 3d regions togther with the fitting before and after CV scan.

The $Na_{10.8}Sn_{1.9}PS_{11.8}$ was further examined as a solid-state electrolyte in a Na-Sn/Na_3PS_4-$Na_{10.8}Sn_{1.9}PS_{11.8}$/$TiS_2$ battery, where Na_3PS_4-$Na_{10.8}Sn_{1.9}PS_{11.8}$ bilayer pellet was used as electrolyte separator. Na_3PS_4 was employed to separate $Na_{10.8}Sn_{1.9}PS_{11.8}$ from Na-Sn anode, avoiding any side reactions. The electrochemical performance of the battery (**Figure 4**) shows a charging capacity of around 120 mAh g^{-1} and a good capacity retention of 92% after 10 cycles, demonstrating $Na_{10.8}Sn_{1.9}PS_{11.8}$ could be applied in all-solid-state batteries.

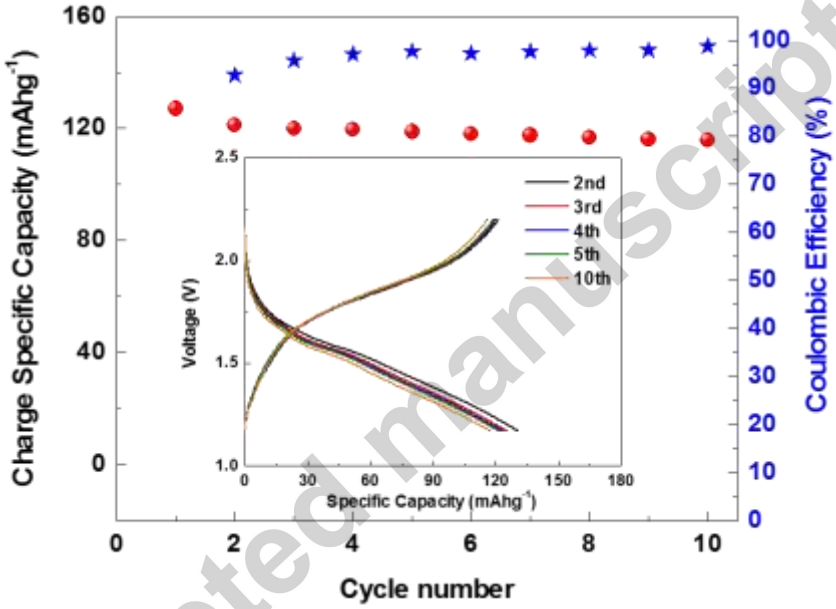

Figure 4. Battery performance of Na-Sn/Na_3PS_4-$Na_{10.8}Sn_{1.9}PS_{11.8}$/$TiS_2$. Cycling performane and voltage profiles of the battery Na-Sn/Na_3PS_4-$Na_{10.8}Sn_{1.9}PS_{11.8}$/$TiS_2$. The battery was characterized at 80 °C under the current density of 4.8 mA g^{-1} (based on the mass of TiS_2), between 1.17 and 2.4 V.

4. Discussion

In order to synthesize phase-pure Na-ion superior conductor Na-Sn-P-S, the Sn/P ratio in the as-prepared materials was systematically tuned, as shown in Figure S8. Impurity phase Na_3PS_4 is detected in the as-prepared $Li_{10}GeP_2S_{12}$-type $Na_{10}SnP_2S_{12}$, which is consistent with the previous study [41]. The amount of impurity phase Na_3PS_4 keeps decreasing with increasing the Sn/P ratio. When the ratio reaches to 1.9, no impurities are detected in the product $Na_{10.8}Sn_{1.9}PS_{11.8}$, indicating that a phase-pure compound has been successfully developed. In addition, first-

principle and phonon calculations show that $Na_{10.8}Sn_{1.9}PS_{11.8}$ is both dynamically and thermodynamically stable. Figure S2 shows the first-principles calculated phonon density of states of $Na_{11}Sn_2PS_{12}$ (Str2, see Table S3) in comparison with those of Na_3PS_4 and Na_4SnS_4 (see Table S5 for their structures), indicating $Na_{11}Sn_2PS_{12}$ is dynamically stable without imaginary modes and $Na_{10.8}Sn_{1.9}PS_{11.8}$ is even more stable due to more intrinsic vacancies (see Table S2). In comparison, the $Li_{10}GeP_2S_{12}$-type $Na_{10}SnP_2S_{12}$ is dynamically unstable with imaginary phonon modes based on our ancillary calculations. First-principles calculations show that $Na_{11}Sn_2PS_{12}$ is also thermodynamically stable with respect to Na_3PS_4 and Na_4SnP_4 at zero K, and it becomes more stable at finite temperatures due to vibrational and especially configurational entropies, indicating again the beneficial role of Na-vacancies to stabilize $Na_{11}Sn_2PS_{12}$ as well as $Na_{10.8}Sn_{1.9}PS_{11.8}$ (Supporting Information Figure S3). By means of the results from single crystal X-ray diffraction, first-principles phonon, and first-principles thermodynamics, it conclusive that the present $Na_{10.8}Sn_{1.9}PS_{11.8}$ is more stable at finite temperatures stemmed mainly from configurational entropy due to vacancies.

A high ionic conductivity in $Na_{10.8}Sn_{1.9}PS_{11.8}$ is mainly attributed to the 3-D Na-ion conduction pathways and intrinsic Na-ion vacancies. After examination of AIMD simulations, the isosurface of Na-ion probability density (see Figure S1b) indicates that Na-ion will diffuse along all possible pathways in the $Na_{10.8}Sn_{1.9}PS_{11.8}$ lattice, for example, the *a*-, *b*-, and *c*-axis as well as the *a/c*-, *b/c*-, and *a/b*-axis directions, showing more Na-ion diffusion channels in $Na_{10.8}Sn_{1.9}PS_{11.8}$ than that in the $Li_{10}GeP_2S_{12}$-type superionic conductor $Na_{10}SnP_2S_{12}$ due partially to more vacancies existed in the $Na_{10.8}Sn_{1.9}PS_{11.8}$ (see Table S2) [41]. It is also noticed that the activation energy Q^{Expt} = 0.307 eV for the $Na_{10.8}Sn_{1.9}PS_{11.8}$ with an ionic conductivity σ = 0.67 mS cm^{-1} (see Figure 2), is higher than the Q^{Expt} = 0.289 eV for Na_3PS_4 with σ = 0.2 ~ 0.4 mS cm^{-1} [34]. It is uncommon that $Na_{10.8}Sn_{1.9}PS_{11.8}$ possesses both high ionic conductivity and high activation energy. It is worth mentioning that ionic diffusivity D and conductivity σ are determined by parameters such as activation energy Q and diffusion prefactor D_0: $\sigma \propto D = D_0 \exp(-Q/k_B T)$ with k_B the Boltzmann's constant and T the temperature (see Section 4 in Supporting Information). Considering the diffusion prefactor D_0 relates to the concentration of Na-vacancy (C_V) in the structure (see Section 4 in Supporting Information), a large number of intrinsic Na-vacancies is believed to be a key reason to enhance Na-ion conductivity in $Na_{10.8}Sn_{1.9}PS_{11.8}$.

5. Conclusions

In summary, a Na-ion SSE $Na_{10.8}Sn_{1.9}PS_{11.8}$ with a unique crystal structure in space group $I4_1/acd$ has been successfully discovered. This $Na_{10.8}Sn_{1.9}PS_{11.8}$ phase possesses a large number of Na-vacancies and 3-D Na-ion conduction pathways. Thus, it exhibits a high ionic conductivity of 0.67 mS cm^{-1} at 25 °C. This $Na_{10.8}Sn_{1.9}PS_{11.8}$ phase is thermodynamically and dynamically stable, but is reduction unstable against Na metal. A Na_3PS_4-$Na_{10.8}Sn_{1.9}PS_{11.8}$ bilayer pellet was used as electrolyte separator and successfully demonstrated the potential applications of $Na_{10.8}Sn_{1.9}PS_{11.8}$ in all-solid-state NIBs. The discovery of this new phase is believed to open a new avenue to develop new SSEs with high ionic conductivity.

ACKNOWLEDGMENTS

The authors acknowledge financial support from the U.S. Department of Energy's (DOE's) Office of Electricity Delivery & Energy Reliability (OE) (under Contract No. 70247), the National Science Foundation (NSF) with Grant No DMR-1610430, and the Penn State 2017 ICS Seed Grant. First-principles calculations were carried out partially on the LION clusters at the Pennsylvania State University, partially on the resources of NERSC supported by the Office of Science of the U.S. DOE under contract no. DE-AC02-05CH11231, and partially on the resources of XSEDE supported by NSF with Grant no. ACI-1053575.

Appendix A. Supporting Information.

Structure of $Na_{10.8}Sn_{1.9}PS_{11.8}$ for first-principles calculations; Details of first-principles, phonon and AIMD calculations; Thermodynamic properties from first-principles and phonon calculations; Single crystal X-ray data collection, structure solution, and refinement data of $Na_{10.8}Sn_{1.9}PS_{11.8}$; XPS depth profile of the pristine $Na_{10.8}Sn_{1.9}PS_{11.8}$ before CV characterization; XRD patterns of as-prepared Na_3PS_4, $Na_{10}SnP_2S_{12}$, $Na_{10.5}Sn_{1.5}P_{1.5}S_{12}$, and $Na_{10.8}Sn_{1.9}PS_{11.8}$; Cross-sectional SEM image of $Na_{10.8}Sn_{1.9}PS_{11.8}$.

Reference

[1] J.M. Tarascon, M. Armand, Nature, 414 (2001) 359-367.
[2] B. Dunn, H. Kamath, J.M. Tarascon, Science, 334 (2011) 928-935.
[3] S. Chen, C. Wu, L. Shen, C. Zhu, Y. Huang, K. Xi, J. Maier, Y. Yu, Adv Mater, (2017) 1700431-1700451.
[4] F. Diaz-Gonzalez, A. Sumper, O. Gomis-Bellmunt, R. Villafafila-Robles, Renew Sust Energ Rev, 16 (2012) 2154-2171.
[5] D. Kundu, E. Talaie, V. Duffort, L.F. Nazar, Angew Chem Int Edit, 54 (2015) 3431–3448.
[6] F.Y. Cheng, J. Liang, Z.L. Tao, J. Chen, Adv Mater, 23 (2011) 1695–1715.
[7] Y.F. Li, D.D. Wang, Q.Y. An, B. Ren, Y.G. Rong, Y. Yao, J Mater Chem A, 4 (2016) 5402-5405.
[8] M.H. Braga, J.A. Ferreira, A.J. Murchison, J.B. Goodenough, J Electrochem Soc, 164 (2017) A207-A213.
[9] Y. An, Z. Zhang, H. Fei, S. Xiong, B. Ji, J. Feng, ACS Appl Mater Interfaces, 9 (2017) 12400-12407.
[10] J. Yue, F. Han, X. Fan, X. Zhu, Z. Ma, J. Yang, C. Wang, ACS Nano, 11 (2017) 4885–4891.
[11] A. Ponrouch, E. Marchante, M. Courty, J.M. Tarascon, M.R. Palacin, Energy Environ Sci, 5 (2012) 8572-8583.
[12] Y. Shi, H. Ha, A. Al-Sudani, C.J. Ellison, G.H. Yu, Adv Mater, 28 (2016) 7921–7928.
[13] S.Y. Wei, S. Choudhury, J. Xu, P. Nath, Z.Y. Tu, L.A. Archer, Adv Mater, 29 (2017) 1605512-1605519.
[14] X.B. Cheng, R. Zhang, C.Z. Zhao, F. Wei, J.G. Zhang, Q. Zhang, Adv Sci, 3 (2016) 201500213-201500232.
[15] N. Kamaya, K. Homma, Y. Yamakawa, M. Hirayama, R. Kanno, M. Yonemura, T. Kamiyama, Y. Kato, S. Hama, K. Kawamoto, A. Mitsui, Nat Mater, 10 (2011) 682-686.
[16] M.H. Braga, A.J. Murchison, J.A. Ferreira, P. Singh, J.B. Goodenough, Energy Environ Sci, 9 (2016) 948-954.
[17] X. Han, Y. Gong, K. Fu, X. He, G.T. Hitz, J. Dai, A. Pearse, B. Liu, H. Wang, G. Rubloff, Y. Mo, V. Thangadurai, E.D. Wachsman, L. Hu, Nat Mater, 16 (2017) 572-579.
[18] Y. Kato, S. Hori, T. Saito, K. Suzuki, M. Hirayama, A. Mitsui, M. Yonemura, H. Iba, R. Kanno, Nat Energy, 1 (2016) 16030.
[19] F.D. Han, T. Gao, Y.J. Zhu, K.J. Gaskell, C.S. Wang, Adv Mater, 27 (2015) 3473–3483.
[20] X.X. Zeng, Y.X. Yin, N.W. Li, W.C. Du, Y.G. Guo, L.J. Wan, J Am Chem Soc, 138 (2016) 15825-15828.
[21] Y.J. Nam, S.J. Cho, D.Y. Oh, J.M. Lim, S.Y. Kim, J.H. Song, Y.G. Lee, S.Y. Lee, Y.S. Jung, Nano Lett, 15 (2015) 3317-3323.
[22] R.D. Shannon, Acta Crystallogr A, 32 (1976) 751-767.
[23] V.S. Kandagal, M.D. Bharadwaj, U.V. Waghmare, J Mater Chem A, 3 (2015) 12992-12999.
[24] A. Hayashi, K. Noi, A. Sakuda, M. Tatsumisago, Nat Commun, 3 (2012) 856.
[25] C.H. Zhang, S. Gamble, D. Ainsworth, A.M.Z. Slawin, Y.G. Andreev, P.G. Bruce, Nat Mater, 8 (2009) 580-584.
[26] O. Bohnke, S. Ronchetti, D. Mazza, Solid State Ion, 122 (1999) 127-136.
[27] K.B. Hueso, M. Armand, T. Rojo, Energy Environ Sci, 6 (2013) 734-749.
[28] Z.Y. Wen, Y.Y. Hu, X.W. Wu, J.D. Han, Z.H. Gu, Adv Funct Mater, 23 (2013) 1005–1018.
[29] Z.G. Yang, J.L. Zhang, M.C.W. Kintner-Meyer, X.C. Lu, D.W. Choi, J.P. Lemmon, J. Liu, Chem Rev, 111 (2011) 3577-3613.
[30] J.J. Wei, H. Kim, D.C. Lee, R.Z. Hu, F.X. Wu, H.L. Zhao, F.M. Alamgir, G. Yushin, J Power Sources, 294 (2015) 494-500.
[31] J.C. Bachman, S. Muy, A. Grimaud, H.H. Chang, N. Pour, S.F. Lux, O. Paschos, F. Maglia, S. Lupart, P. Lamp, L. Giordano, Y. Shao-Horn, Chem Rev, 116 (2016) 140-162.
[32] A. Hayashi, K. Noi, N. Tanibata, M. Nagao, M. Tatsumisago, J Power Sources, 258 (2014) 420-423.
[33] N. Tanibata, K. Noi, A. Hayashi, N. Kitamura, Y. Idemoto, M. Tatsumisago, ChemElectroChem, 1 (2014) 1130-1132.

[34] Z. Yu, S.-L. Shang, J.-H. Seo, D. Wang, X. Luo, Q. Huang, S. Chen, J. Lu, X. Li, Z.-K. Liu, D. Wang, Adv Mater, 29 (2017) 1605561-1605567.
[35] S.L. Shang, Z.X. Yu, Y. Wang, D.H. Wang, Z.K. Liu, ACS Appl Mater Interfaces, 9 (2017) 16261-16269.
[36] L. Zhang, K. Yang, J.L. Mi, L. Lu, L.R. Zhao, L.M. Wang, Y.M. Li, H. Zeng, Adv Energy Mater, 5 (2015) 1501294-1501298.
[37] A. Banerjee, K.H. Park, J.W. Heo, Y.J. Nam, C.K. Moon, S.M. Oh, S.-T. Hong, Y.S. Jung, Angew Chem Int Edit, 55 (2016) 9634-9638.
[38] H. Wang, Y. Chen, Z.D. Hood, G. Sahu, A.S. Pandian, J.K. Keum, K. An, C. Liang, Angew Chem Int Edit, 55 (2016) 8551-8555.
[39] I.-H. Chu, C.S. Kompella, H. Nguyen, Z. Zhu, S. Hy, Z. Deng, Y.S. Meng, S.P. Ong, Sci Rep, 6 (2016) 33733.
[40] P. Bron, S. Johansson, K. Zick, J.S. auf der Gunne, S. Dehnen, B. Roling, J Am Chem Soc, 135 (2013) 15694-15697.
[41] W.D. Richards, T. Tsujimura, L.J. Miara, Y. Wang, J.C. Kim, S.P. Ong, I. Uechi, N. Suzuki, G. Ceder, Nat Commun, 7 (2016) 11009.
[42] C.W. Glass, A.R. Oganov, N. Hansen, Comput Phys Commun, 175 (2006) 713-720.
[43] G. Kresse, J. Furthmuller, Phys Rev B, 54 (1996) 11169-11186.
[44] Y. Wang, S.-L. Shang, H. Fang, Z.-K. Liu, L.-Q. Chen, npj Comput Mater, 2 (2016) 16006.
[45] S.L. Shang, Y. Wang, D. Kim, Z.K. Liu, Comp Mater Sci, 47 (2010) 1040-1048.
[46] K. Momma, F. Izumi, J Appl Crystallogr, 44 (2011) 1272-1276.
[47] M. Duchardt, U. Ruschewitz, S. Adams, S. Dehnen, B. Roling, Angew Chem Int Edit, 57 (2018) 1351-1355.
[48] Z. Zhang, E. Ramos, F. Lalere, A. Assoud, K. Kaup, P. Hartman, L.F. Nazar, Energy Environ Sci, 11 (2018) 87-93.
[49] W. Stelte, J.K. Holm, A.R. Sanadi, S. Barsberg, J. Ahrenfeldt, U.B. Henriksen, Fuel, 90 (2011) 3285-3290.
[50] B.J. Neudecker, W. Weppner, J Electrochem Soc, 143 (1996) 2198-2203.
[51] S. Wenzel, T. Leichtweiss, D.A. Weber, J. Sann, W.G. Zeier, J. Janek, ACS Appl Mater Interfaces, 8 (2016) 28216-28224.
[52] S. Wenzel, S. Randau, T. Leichtweiss, D.A. Weber, J. Sann, W.G. Zeier, J. Janek, Chem. Mater., 28 (2016) 2400-2407.

Graphical abstract

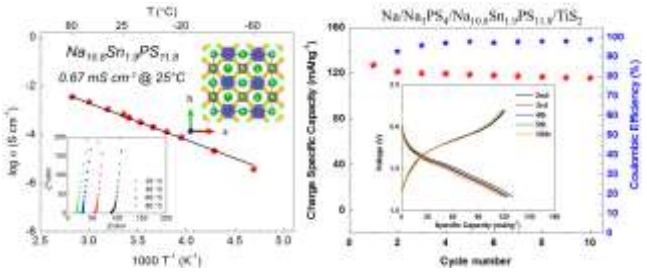

Bio-sketch: Zhaoxin Yu

Zhaoxin Yu received his B.S. (2009) and M.S. (2012) degrees in Materials Science and Engineering from University of Science and Technology Beijing, and Ph.D. (2017) degree in Department of Mechanical and Nuclear Engineering from The Pennsylvania State University, under the direction of Dr. Donghai Wang. He is presently a postdoctoral researcher in Dr. Donghai Wang's Energy Nanostructure (E-Nano) lab. His research interests include synthesis and structure-property relationships of materials for energy conversion and storage.

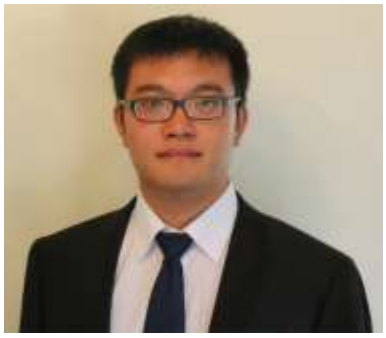

Bio-sketch: Shun-Li Shang

Dr. Shun-Li Shang is a Research Professor at the Pennsylvania State University's Department of Materials Science and Engineering since 2017. After receiving his PhD in materials and metallurgy from the General Research Institute for Nonferrous Metals, Beijing, China, he joined Delft University of Technology, Netherlands, in 2002, and then, Pennsylvania State University, in 2005 for postdoctoral studies. Dr. Shang's research interests include computational thermodynamics, first-principles, and phonon calculations to study thermodynamic, diffusion, and mechanical properties of ordered and disordered alloys, compounds, and functional materials. He has published over 200 peer-reviewed papers with an H-index of 37 (Google Scholar).

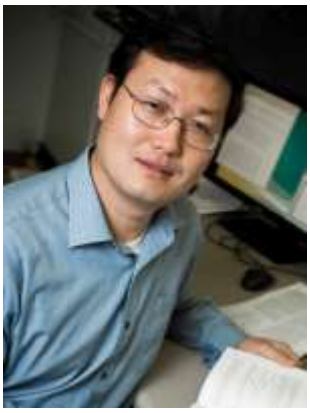

Bio-sketch: Yue Gao

Yue Gao is currently a doctoral student in Department of Chemistry, the Pennsylvania State University, working in Dr. Donghai Wang's Energy Nanostructure (E-Nano) lab. He received his B.S. (2012) in School of Chemistry and Chemical Engineering, Lanzhou University, China. His current research focuses on constructing the stable interface for energy storage material.

Bio-sketch: Daiwei Wang

Daiwei Wang received his B.S. (2015) in Chemical Engineering from Tsinghua University, China. He is currently a Ph.D. candidate in Department of Mechanical and Nuclear Engineering, The Pennsylvania State University, working in Dr. Donghai Wang's Energy Nanostructure (E-Nano) lab. His research focuses on synthesis of materials for energy storage and energy conversion.

Bio-sketch: Xiaolin Li

Dr. Xiaolin Li is a senior scientist at Pacific Northwest National Laboratory. He received his Ph.D. degree in 2005 from Department of Chemistry, Tsinghua University and conducted his postdoctoral research in Hongjie Dai's group at Stanford University. He has extensive experience with carbon nanotubes, graphene, and is an expert in designing nanostructured functional materials for various applications. His current research interest is on battery materials and renewable energy. He has authored/co-authored more than 70 papers, which have been cited for more than 20,000 times. His h-index is 50.

Bio-sketch: Zi-Kui Liu

Dr. Zi-Kui Liu is a distinguished professor in the department of Materials Science and Engineering at The Pennsylvania State University. He obtained his BS from Central South University (China), MS from University of Science and Technology Beijing (China), PhD from Royal Institute of Technology (KTH, Sweden). Dr. Liu was a research associate at University of Wisconsin-Madison and a senior research scientist at Questek Innovation, LLC. His current research activities are centered on first-principles calculations, modeling of thermodynamic, kinetic and other physical/chemical properties, and their integration in understanding defects, phase stability, phase transformations, and design of materials processing and properties.

Bio-sketch: Donghai Wang

Dr. Donghai Wang is currently Associate Professor at Department of Mechanical Engineering and Department of Chemical Engineering at The Pennsylvania State University. Before joining Penn State in 2009, he was a postdoc and subsequently became a staff scientist at Pacific Northwest National Laboratories where he developed functional materials for catalysis and energy storage techniques. He received a B.S. and Ph.D. degree in Chemical Engineering from Tsinghua University and Tulane University in 1997 and 2006, respectively. Dr. Donghai Wang's research interests have been related to design and synthesis of materials for a variety of applications. His recent research is focused on material development for energy conversion and storage technologies such as batteries, supercapacitors, fuel cells and solar fuels. Professor Wang has authored and co-authored over 90 peer reviewed publications, more than 15 patents and patent applications, and 4 book chapters.

Highlights:

1. $Na_{10.8}Sn_{1.9}PS_{11.8}$ has been discovered with the new crystal structure (space group $I4_1/acd$).
2. $Na_{10.8}Sn_{1.9}PS_{11.8}$ phase exhibits a high ionic conductivity of 0.67 mS cm^{-1} at 25 °C.
3. High ionic conductivity is due to the intrinsic Na vacancies and 3-D Na-ion conduction pathways.